Overview of TJ-II experiments

IOP Publishing and International Atomic Energy Agency Nuclear Fusion

Nucl. Fusion **51** (2011) 094022 (10pp) doi:10.1088/0029-5515/51/9/094022

Overview of TJ-II experiments

J. Sánchez, M. Acedo, D. Alegre, A. Alonso, J. Alonso, P. Álvarez, J. Arévalo, E. Ascasíbar, A. Baciero, D. Baião[1], L. Barrera, E. Blanco, J. Botija, A. Bustos, E. de la Cal, I. Calvo, A. Cappa, D. Carralero, R. Carrasco, B.A. Carreras[2], F. Castejón, R. Castro, G. Catalán, A.A. Chmyga[3], M. Chamorro, L. Eliseev[4], L. Esteban, T. Estrada, J.A. Ferreira, J.M. Fontdecaba, L. García[5], R. García-Gómez, J.M. García-Regaña, P. García-Sánchez, A. Gómez-Iglesias, S. González, J. Guasp, T. Happel, J. Hernanz, J. Herranz, C. Hidalgo, J.A. Jiménez, A. Jiménez-Denche, R. Jiménez-Gómez, I. Kirpitchev, A.D. Komarov[3], A.S. Kozachok[3], L. Krupnik[3], F. Lapayese, M. Liniers, D. López-Bruna, A. López-Fraguas, J. López-Rázola, T. Madeira[1], F. Martín-Díaz, F. Martín-Hernández, A.B. Martín-Rojo, J. Martínez-Fernández, K.J. McCarthy, F. Medina, M. Medrano, L. Melón, A.V. Melnikov[4], P. Méndez, B. van Milligen, E. Mirones, A. Molinero[6], M. Navarro, I.S. Nedzelskiy[1], M. Ochando, J. Olivares, E. Oyarzábal, J.L. de Pablos, L. Pacios, I. Pastor, M.A. Pedrosa, A. de la Peña, A. Pereira, A. Petrov[4], S. Petrov[7], A. Portas, G. Rattá, J.M. Reynolds[8], E. Rincón, L. Ríos, C. Rodríguez, B. Rojo, J.A. Romero, A. Ros, M. Sánchez, E. Sánchez, G. Sánchez-Burillo, E. Sánchez-Sarabia, K. Sarksian[9], J.A. Sebastián, C. Silva[1], E.R. Solano, A. Soleto, F. Tabarés, D. Tafalla, J. Tera, A. Tolkachev, J. Vega, G. Velasco, J.L. Velasco, M. Weber, G. Wolfers and B. Zurro

Laboratorio Nacional de Fusión, Asociación EURATOM/CIEMAT, 28040, Madrid, Spain
[1] Associação EURATOM/IST, Instituto de Plasmas e Fusão Nuclear. Av. Rovisco Pais, 1049-001 Lisboa. Portugal
[2] BACV Solutions Inc., Oak Ridge, TN 37830, USA
[3] Institute of Plasma Physics, NSC KIPT, 310108 Kharkov, Ukraine
[4] Institute of Nuclear Fusion, RNC Kurchatov Institute, Moscow, Russia
[5] Universidad Carlos III, Madrid, Spain
[6] Laboratorio General de Electrónica y Automática–CIEMAT, Miguel Navarro Santana
[7] A.F. Ioffe Physical Technical Institute, 26 Polytekhnicheskaya, St Petersburg, Russia
[8] BIFI, Universidad de Zaragoza, 50009-Zaragoza, Spain
[9] General Physics Institute, Russian Academy of Sciences, Moscow, Russia

E-mail: joaquin.sanchez@ciemat.es

Received 29 December 2010, accepted for publication 28 July 2011
Published 31 August 2011
Online at stacks.iop.org/NF/51/094022

Abstract
This paper presents an overview of experimental results and progress made in investigating density control using Li-coating, transport and L–H transitions in TJ-II. The Li-coating changes drastically the plasma–wall interaction, decreasing the recycling, and enlarges substantially the operational range of the device delaying the appearance of radiative collapse that happens for higher densities, which permits confinement properties of much denser plasmas to be studied. Moreover, L–H mode transition has only been achieved after Li-coating in TJ-II. The effect of rational surfaces on heat transport is studied showing a decrease in heat diffusivity close to their position, and it is also seen that rational surfaces located in the edge make L–H transition easier. TJ-II findings provide a new guideline for understanding the trigger mechanism of the L–H transition pointing out the importance of low frequency fluctuating sheared $E \times B$ flows. The properties of fast-ion confinement are described as well as the effects of impurities on radiation profiles, showing two types of profiles the *bell* and the *dome* shape, the latter being more prone to radiative collapse.

(Some figures in this article are in colour only in the electronic version)

1. Introduction

Global confinement and accessibility to improved confinement regimes are strongly linked to the magnetic topology in fusion plasmas. The flexibility of stellarator devices makes them ideal laboratories to study the relation between magnetic topology, electric fields and transport. In particular, the specific characteristics of the stellarator TJ-II, i.e. low magnetic shear and high magnetic configuration flexibility in the plasma shape and volume and, especially, in the iota profile, allow controlling the position of low order rational values within the rotational transform profile and, therefore, the study of how the magnetic topology affects transport and global confinement. On top of the topology influence on confinement a research on the influence of Li wall coating on confinement is also performed. The main properties of plasma–wall interaction under Li-wall-coated conditions are therefore explored. In the line of improvement of confinement, an effort is also done in stellarator optimization in order to find an optimized stellarator configuration with the same flexibility properties as TJ-II [1].

Recent improvements in plasma diagnostics have led to a better understanding of the confinement properties of TJ-II, including a two-channel Doppler reflectometer for electric field and density turbulence studies [2], heavy ion beam probe (HIBP) diagnostic for the characterization of plasma potential, plasma density and their fluctuations [3], diagnostics for long-range correlation studies making use of two fast reciprocating Langmuir probe arrays located at two different toroidal positions [4], supersonic He beam for ion temperature measurements [5], suprathermal ion detection by spectroscopy and luminescent probe [6], the development of a dedicated neutral beam injection (NBI) system and charge-exchange diagnostic [7], two-colour infrared interferometer [8], implementation of multi-filter photodiodes for core electron temperatures [9] and advanced data processing techniques [10].

The results presented in this paper were obtained in plasmas created and heated by electron cyclotron resonance heating (ECRH) (2×300 kW gyrotrons, at 53.2 GHz, second harmonic, X-mode polarization) and NBI. The ECRH was coupled to the plasma via two quasi-optical transmission lines, placed at stellarator-symmetric positions, equipped with an internal steerable mirror. Beams of 400 kW port-through (H_0) power at 30 kV were injected into target plasmas created using one or both gyrotrons. Ongoing TJ-II experiments are focussed on studying the efficiency of the electron Bernstein waves (EBW) heating system using the O–X–B mode conversion scenario. Those waves are also very efficient at driving non-inductive currents due to the fact that they resonate with fast low-collisional electrons, and hence can modify the rotational transform profile and compensate the bootstrap current [11], with the limitation of the small control one has on the power deposition profile. The estimates of the bootstrap current, which is very challenging for the complex TJ-II geometry, have been performed [12] in order to have a prediction of the current to be compensated by EBCD.

The paper is organized as follows: in section 2, the role of Li-coating on TJ-II particle control is discussed. Confinement and configuration effects are discussed in section 3. L–H transition in TJ-II is discussed in section 4. Finally, conclusions are presented in section 5.

2. Li-coating experiments and particle control by gas injection

Great improvement of plasma particle control has been achieved in the TJ-II stellarator after Li-coating [13], in comparison with the operation under Boron-coated walls. Although a systematic improvement on plasma operation has been reported for basically all kinds of fusion devices [14], the beneficial Li properties for plasma–wall interaction have an enhanced effect on this device, possibly due to the fact that it presents a helical limiter very close to the magnetic axis, which receives the strongest particle and heat fluxes. The groove of the vacuum chamber is in fact in contact with the plasma, thus acting as a limiter that follows a four period circular helix. In boron-coated wall plasmas a systematic, steady density ramp up was observed as the beam power was switched on. This fast density build-up, being limited to the available heating power, led generally to a relatively quick plasma termination due to radiative collapse, for line density values below 3×10^{19} m^{-3}. Under lithium conditions the density control has been dramatically improved and long, stationary density plateaus (up to ten energy confinement times) can be achieved, allowing density scans with the help of external gas puff, as shown in figure 1 [15]. This figure illustrates the difference between both wall scenarios as regards the behaviour of energy content and confinement time, both for ECR and NBI discharges using the co-injector with comparable heating power and the same magnetic configuration. In order to get some insight into the underlying physics, a systematic comparison of the global particle and energy balance under both wall scenarios and otherwise identical main plasma parameters has been recently addressed. It was concluded that for the overlapping parametric space, and in particular for ECR heated plasmas, no major difference in the zero-dimensional analysis can be seen, while much better confinement is found in high density plasmas for Li coating conditions.

In the last campaigns, an important effort has been devoted to the understanding of sputtering and retention characteristics of the Li layers, and their possible interconnection [16]. The very low value of H recycling under the film coating technique used in TJ-II (Li on top of a B layer), given by a recycling coefficient as low as $R \sim 0.1$, warrants density control in gas puffed or NBI fuelled plasmas, as it has been described in [13]. For He plasmas, values as low as $R \sim 0.82$ have been deduced from steady state or perturbative puffing experiments with He at room temperature ($T < 325$ K). Recently, desorption of H trapped into the Li film by the He plasma discharge has been addressed. Of particular interest is to check whether a He plasma ejects both species from the film (H and Li) with similar or distinct energy threshold and yields. In the first case, the sputtering of some sort of molecular entity (such as LiH for example) would be expected, the resulting individual emissions being produced by plasma fragmentation. In contrast, although similar absolute values for the corresponding yields are predicted by the TRIM code for a pure Li layer [16], different energy dependence should be observed, as one could deduce from different threshold values. However, the fact that strong material mixing is expected upon plasma exposure of the coating, leading to surface dilution

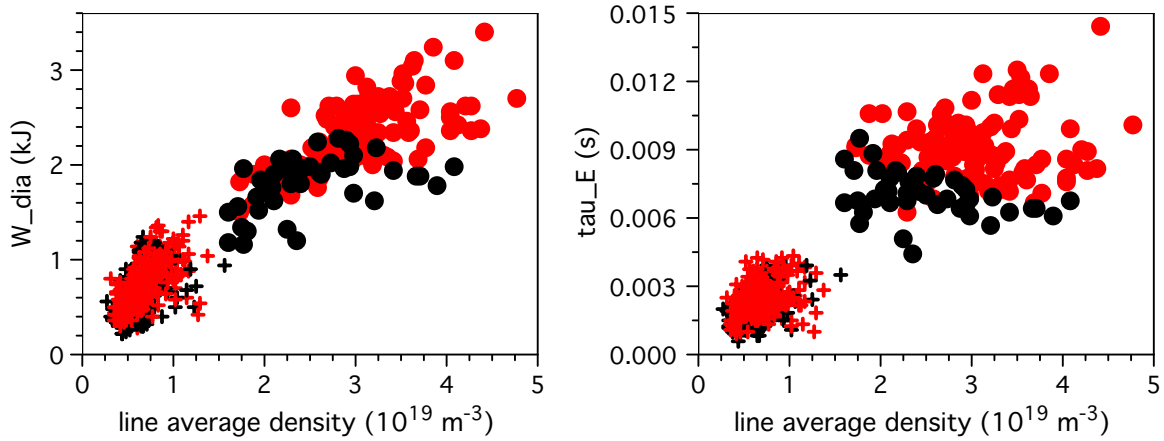

Figure 1. Maximum value of the plasma energy content (left) and energy confinement time (right) versus plasma density for B-coated (black) and Li-coated walls (red symbols). Crosses correspond to ECR and circles correspond to NBI heated discharges.

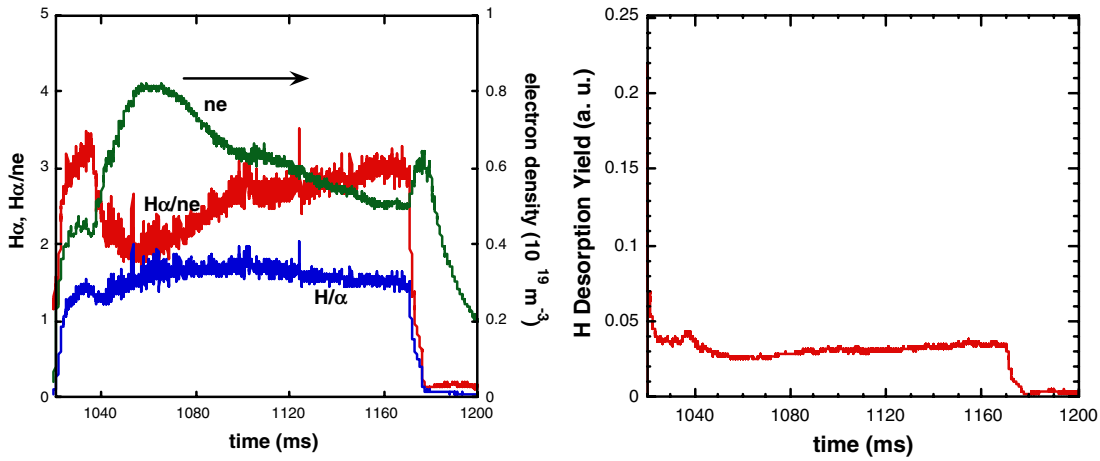

Figure 2. Left panel: time traces of H_α (lower trace), electron density (right) and ratio between them (upper trace, left) for a He, ECRH plasma on a hydrogenated Li wall. Right panel: deduced hydrogen desorption yield for He on Li : H for the same discharge.

and chemical bonding effects, makes it very difficult to assess how the ratio of H to Li ejection should behave in reality. Furthermore, the ratio of neutral to ionic sputtering yields, assumed to be 1/3 for metallic lithium [17], could be strongly modified by the presence of more electronegative species (such as carbon and boron) in the mixture. In figure 2, the release of H by He plasma (b) and the line average density together with the density-normalized H_α emission (a) are depicted. A fairly constant yield of $\gamma \sim 0.03$–0.04 is deduced for this particular discharge. The analysis of other similar discharges yields values between 0.02 and 0.06, in very good agreement with TRIM code estimates and making allowance for the intrinsic uncertainties in the estimates.

Figure 3 shows the dependence of the Li emission and the H_α signal, both density-normalized, on the electron temperature at the last closed flux surface, as measured by the He beam diagnostic in the same toroidal location [16]. Two important facts are worth highlighting in the data shown in the figure. First, a very similar threshold energy, corresponding to electron temperatures of $T_e \sim 50$ eV, seems to exist for both processes, obviously higher than the expected ones from TRIM calculations ($E_{th} \sim 9$ eV for Li sputtering by He^+). Second, the same energy dependence seems to apply for H desorption and Li sputtering, two distinct processes in terms of standard sputtering theory.

Finally, the release of glow-discharge-implanted He by a H plasma normalized to the particle flux was followed in a shot to shot basis [16]. The results are shown in figure 4 and were obtained by the measurement of the emission of He (at 667 nm) in the plasma and by mass spectrometry, using a residual gas analyser (RGA) that measures the composition of the residual gas in the vacuum chamber. As seen in the figure, a transient phase characterized by a time constant of 0.5 s (∼2 shots) is followed by a steady value of He desorption after a few shots. This behaviour was also apparent during glow-discharge conditioning of a He saturated Li wall by a H plasma and is interpreted as a diffusion-limited release process, thus implying that refilling of the topmost layer, which is He-depleted by H bombardment in every shot, takes place between shots. Experiments with different time delays between shots are now in progress in order to characterize the corresponding diffusion coefficient.

A key ingredient for understanding the operational improvement is the radiation profile under Li-coated wall. Edge radiation can be kept small avoiding the power unbalance that triggers the low radiation collapse. This type of collapse

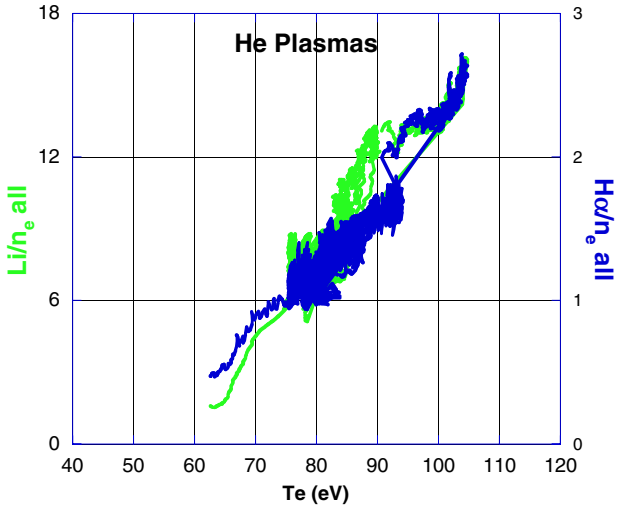

Figure 3. Dependence of the Li emission and Hα signal, both density-normalized, with the LCFS electron temperature.

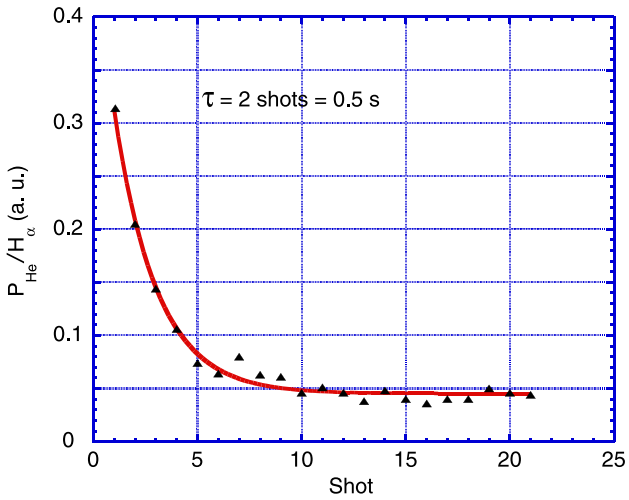

Figure 4. Shot by shot evolution of the release of He, normalized to the plasma flux (H_α signal), in H plasmas. It is seen that the final value of desorbed gas (as measured by RGA) is saturated probably due to a diffusion process in the wall. The typical decay constant, τ, is also shown in the figure.

is characterized by the fact that the total radiated power is less than the absorbed one and just a local unbalance triggers the collapse [18]. It has been observed that these profiles (with strong pressure gradients and enhanced central confinement, concomitant to central impurity accumulation) transited spontaneously to broader profiles (with lower-central $Z_{\rm eff}$ values) when the density limit is approaching. Radiation profile shapes have been tagged as *bell* and *dome* type, respectively, and the transition between them during a shot is regularly classified and followed from bolometric data. Perturbative experiments (using H_2, mixtures of H_2 + Ne, and N_2 gas injection) were performed to force the bell-to-dome profile transition at moderate densities, far from the 'spontaneous' transition conditions (see figure 5). The detailed dynamics of profile change consisted in an almost simultaneous edge increase and core decrease of radiation, and it was essentially the same under diluted Ne or H_2 injections. Hence, the observed decrease in the peaking factor cannot be attributed to simultaneous and different increases in the radiation in the core and in the edge. This response was found compatible with enhanced peripheral charge-exchange processes that diminish the coupling of fast neutrals with the plasma core (i.e. reduces density peaking), and may favour the development of thermal instability-driven plasma collapse.

With the aim of trying to find a method to control the density rise through the reduction of wall sputtering via edge radiation cooling, during the last experimental campaign, other non-intrinsic low-Z impurity species, namely N_2, has been injected. What was observed is that adequate amounts of this impurity may establish a quasi-stationary radiation enhanced region at the plasma periphery (see figure 6). Core radiation does not increase immediately, as can be seen in figure 6 for shot #23632, and is explained in [19].

By comparing discharges with injection and their reference shots in different magnetic configurations, we found that the deepest radial location in which we see the maximum positive perturbation in radiation due to impurity penetration varies, and coincides with the nominal location of significant rational surfaces [20]. In the latter reference, a discussion in terms of radiation strength at the plasma periphery led us to conclude that a sort of impurity screening occurred in seeded discharges. Then, we explored different magnetic configurations and compared local emissivities from seeded discharges and from their reference shots. We found that the radial location in which we see the maximum increase in radiation was systematically that of the nominal location of significant rational surfaces in each configuration.

Laser blow-off has been used to inject trace boron impurities to study impurity transport. The parallel transport of boron ions has been measured with two filter-scopes monitoring B II line on opposite sides of the torus. Following the initial fast parallel propagation of boron ions, a slower (above 10 ms) global confinement of impurities has been investigated in ECRH and NBI plasmas. Boron confinement times are similar to those previously observed for Fe [21].

3. Confinement and configuration effects

The TJ-II is a low magnetic shear device. It is therefore very important to know at what extent low order rational values of the rotational transform (magnetic resonances) alter the plasma properties. This has been done following their possible effect on the electron temperature profiles. ECRH plasmas of the TJ-II Heliac are suited for these studies because (i) they allow electron cyclotron emission measurements to be taken from which the time evolution of the inverse $T_{\rm e}$-gradient ($1/T_{\rm e}'$) can be obtained; and (ii) the discharges can be performed at varying magnetic configuration so as to change the offset of the rotational transform profile at constant plasma volume. In this way, the magnetic resonances move through the plasma during the discharge. To give more physical meaning to the results, the profiles of $1/T_{\rm e}'$ are presented in the form of an effective electron-heat diffusivity, $\chi_{\rm e} = Q_{\rm e}/(nT_{\rm e}'V')$, where $Q_{\rm e}$ is the volume integral of the ECRH power, n is the plasma density and V' is the radial derivative of the plasma volume. The experiments show reduced values of $\chi_{\rm e}$ in regions where the lowest order magnetic resonances are located as the configuration is varied

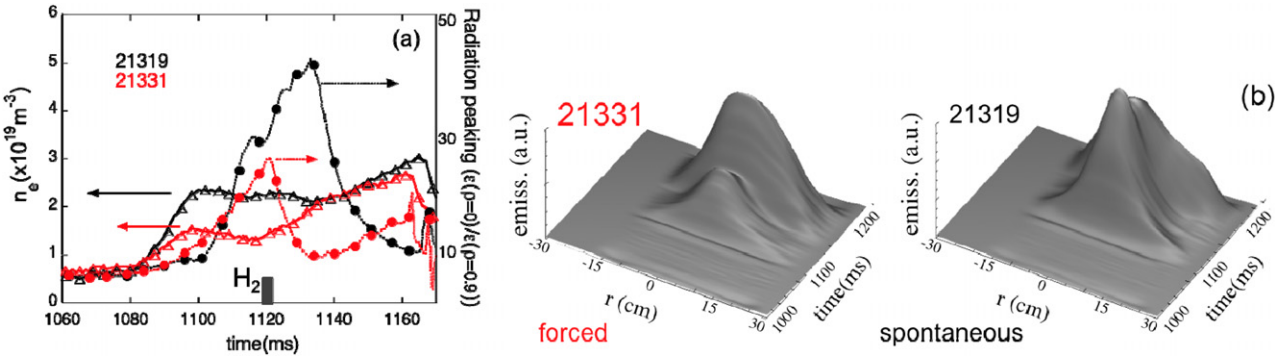

Figure 5. (*a*) Evolution of radiation peaking (defined as the ratio of the emissivities at the centre, $\rho = 0$, and at the periphery, $\rho = 0.9a$, being a the minor radius) and line density, and (*b*) time evolution of emissivity profiles for two shots showing forced (due to a short H_2 pulse injection) and spontaneous transitions.

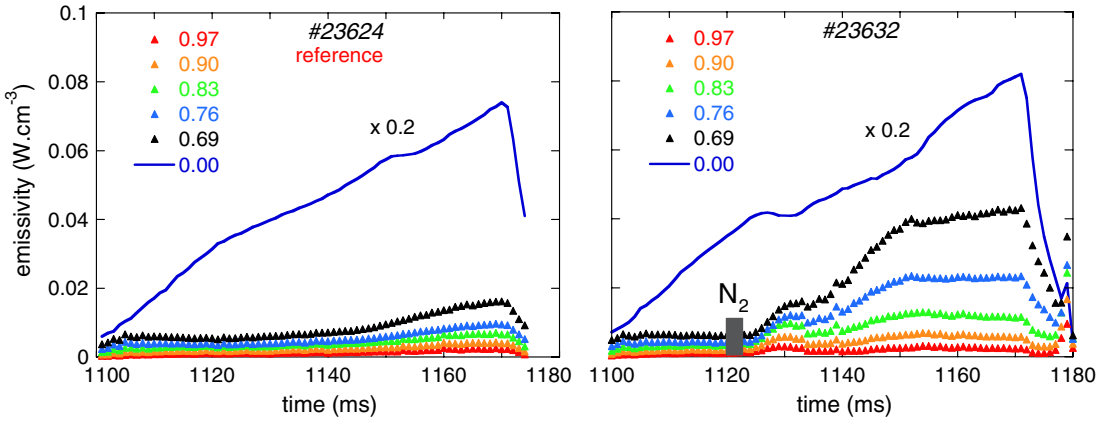

Figure 6. Time evolution of plasma emissivity at the indicated effective radii. The 4 ms length N_2 pulse starts at 1120 ms in shot # 23632.

during the discharge [22]. This is illustrated in figure 7, where χ_e is shown in the form of contour plots as a function of time and minor radius in two symmetric experiments of dynamic configuration scans: in figure 7(*a*) the offset of the rotational transform profile decreases giving rise to an outward movement of the main magnetic resonances through the plasma radius; in figure 7(*b*) the offset increases causing an inward sweeping of the same resonances. The apparent lowering of χ_e (note the scale in the colour bar) coincident with the radial position of the resonances has been found in many repetitions of these dynamic scans, thus providing confidence in the result. Confirming earlier experiments, Doppler reflectometry measurements in the density gradient region, roughly the outer half radius, identify augmented electric fields E_r with the location of magnetic resonances [23], i.e. E_r becomes locally more positive if already positive or tends towards positive values if negative. The results point to kinetic effects due to favoured electron transport in the presence of the resonances: not only the augmented E_r—towards the electron root—changes the neoclassical fluxes, but presumably E_r augments in a narrow radial region, thus creating an $E \times B$ shear-flow layer that may reduce anomalous transport as well. New experiments have been designed to clarify these aspects.

It is worth recalling that TJ-II operates nominally in very low magnetic shear magnetic configurations. The plasmas behave as if the resonances happened in an environment of 'healed' islands, which is part of the motivation to study the healing of islands in helical devices jointly with other devices [24]. Kinetic calculations [25] in the geometry of the standard TJ-II magnetic configuration, based on collisional transport alone, show 3D plasma current densities able to modify the magnetic structure in the resonant regions, even in the absence of electric fields [22]. Both elements, radial electric field and plasma current in the resonant regions, are also important in other phenomena such as the formation of internal electron-heat barriers and have been proposed as tools to control plasma performance.

A transition from the kinetic-effect-dominated regime to a more collisional one is found in ECRH plasmas. The electric field, positive all over the plasma in the low density regime, typical of ECRH plasmas, starts developing negative values at the maximum density gradient region when the collisionality reaches a threshold value. Further increments in the density extend the region with negative electric fields towards the plasma centre. In the lithium-coated NBI plasmas studied in this paper, plasma density has been varied in the range $1.7 \times 10^{19}\,\mathrm{m}^{-3} \leqslant \bar{n}_e \leqslant 6.1 \times 10^{19}\,\mathrm{m}^{-3}$, the energy confinement time, τ_E, ranging from 3 to 14 ms.

During the NBI heating phase broad spectral structures that straddle intense emission lines from multiply ionized oxygen lines are observed by a normal-incidence spectrometer viewing a plasma region well separated from the neutral beam/plasma interaction volume [26]. It has been demonstrated that their source is fast oxygen ions that originate

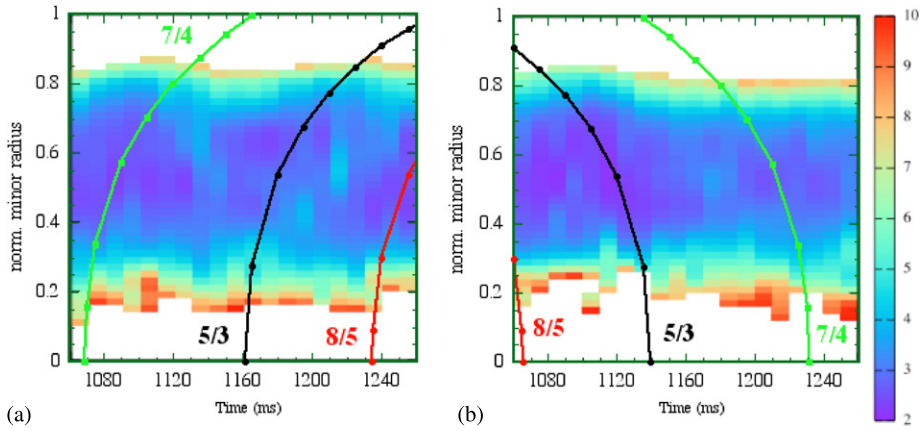

Figure 7. Evolution of effective electron thermal diffusivity (the colour bar is in $m^2\ s^{-1}$) profiles in two dynamic configuration scans at constant volume: (*a*) decreasing rotational transform in TJ-II discharge # 21657; and (*b*) increasing rotational transform in discharge #21663.

as accelerated H_2O and H_3O ions in the ion sources of the NBI. Once neutralized in the neutralization chamber they penetrate the plasma where they are reionized, confined and perform multiple toroidal transits of the TJ-II before being lost or slowed down. On the one hand, these findings have implications for the analysis of oxygen spectral lines during NBI heating phases in TJ-II, and possibly other magnetically confined plasma devices. On the other hand, such emissions may provide a tool for studying phenomena such as fast-ion slow down and confinement, or the influence of NBI injection direction and toroidal magnetic field on fast ions as the observations demonstrate the possibility of employing neutral beams doped with a suitable impurity element, if not already doped with oxygen, in combination with strategically positioned spectroscopic instruments, to probe such behaviour in hot magnetically confined plasmas.

Alfvén eigenmodes (AEs) destabilized in NBI plasmas [27], also related to low order resonances, can influence fast-ion confinement. The dynamics of fast ions coming from NBI is also estimated for TJ-II using the code ISDEP, which allows one to estimate the slowing down time, the confinement and distribution function of these ions in order to compare these results with the CX-NPA measurements [28].

Recently the HIBP system has become a new tool to study AEs with high spatial and frequency resolution [3]. AEs are pronounced in the local density, electric potential and poloidal magnetic field oscillations, detected simultaneously by HIBP in the frequency range $50\,\text{kHz} < f_{\text{AE}} < 300\,\text{kHz}$. Various AE modes are visible in the neutral beam injector (NBI)-heated plasma for co-NBI (<450 kW), counter- (<450 kW) and balanced NBI (<900 kW) from the plasma centre to the edge. A high coherence between magnetic probes and HIBP data was found for specific AEs. When the density rises, AE frequency decreases and the cross-phase between the plasma density, poloidal magnetic field and potential remains constant. The amplitudes of the AE potential oscillations are in the order of 10 V with poloidal electric fields in the order of $1\,\text{kV m}^{-1}$. AEs may bring small or significant contribution to the turbulent $E \times B$ particle flux depending on the amplitudes and cross-phase between density and poloidal electric field fluctuations (see figure 8) [29]. Typically, the particle flux induced by AEs was found to vary widely from a negligibly low level up to being comparable to the flux induced by broadband turbulence.

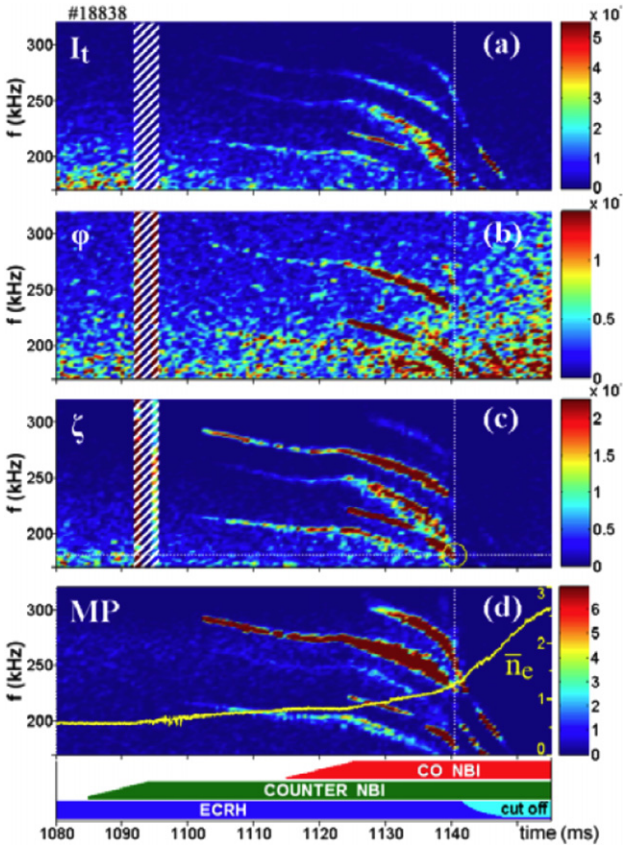

Figure 8. Power spectra time evolution of HIBP ($\rho = 0.5$) and Mirnov probe signals. AEs are clearly observed in (*a*) the total HIBP secondary beam current, I_t, proportional to the plasma density; (*b*) on the potential; (*c*) on the toroidal shift of secondary beam ζ proportional to B_{pol}; (*d*) on the Mirnov probe signal. The line-averaged density is also shown in (*d*). Instrumental gaps in HIBP signal is shown by hatched ribbons in (*a*), (*b*), (*c*).

The theoretical investigation of the possibly destabilized Alfvén waves is done using the codes CONTI and CAS3D (see [27] and references therein). An analysis of the MHD Alfvén spectrum and its interaction with sound waves was performed. Both codes take the actual complex TJ-II equilibria calculated with the VMEC code for the experimental pressure profiles.

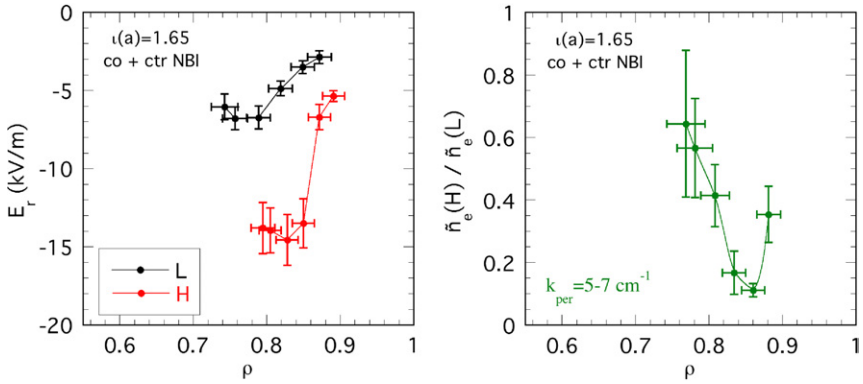

Figure 9. Doppler reflectometry measurement showing: (left) radial electric field profiles measured during the L and H-modes and (right) density fluctuation reduction at the perpendicular wave-number range 5–7 cm^{-1}.

The comparison with the plasma experimental time traces and the corresponding Mirnov coil spectrograms (see figure 8) confirm that the Alfvén mode pattern is mainly determined by the magnetic configuration with the frequency evolution having the expected inverse dependence on the square root of the plasma density. All four mode families, from $N = 0$ to $N = 3$, were included in the study and the $N = 0$ family was the one that compares best with the experimental results. The results obtained so far give some hints about which modes might be visible in the experiment, but a conclusive statement could not be made. Furthermore, it was not clear why among many modes with strong continuum interaction and therefore strong damping, especially those visible in the experiment should be destabilized. Nevertheless further investigation is necessary because a clear identification of modes also requires the experimental determination of toroidal mode numbers and the radial structure of the mode.

4. L–H transition studies

Tokamaks and stellarators develop edge plasma bifurcations with similar properties. In the TJ-II stellarator, spontaneous low to high (L–H) transitions are achieved [30] under NBI heating conditions when operating with lithium-coated walls. H-mode transitions reproduce common features found in other devices: i.e. an increase in plasma density and plasma energy content, a reduction in H_α signal, the development of steep density gradients and a drastic reduction in the level of turbulence. For high-power, high-density plasmas the confinement improvement associated with the L–H transition reaches up to 40%. The radial electric field, as measured by Doppler reflectometry [2], is of the order of 5 $\mathrm{kV\,m^{-1}}$ in the L-mode and increases up to 15 $\mathrm{kV\,m^{-1}}$ in the H-mode with a concomitant development of a strong $E \times B$ sheared flow in the proximity of $\rho \approx 0.85$ [31]. At this radial position the density fluctuation level is reduced by a factor of 10. This reduction being strongly localized at the position of the maximum in the radial electric field shear (see figure 9).

In addition to the observation of a significant sheared radial electric field during the spontaneous L–H transition, an important result is the observation of remarkable fluctuating radial electric fields during the development of edge bifurcations [30]. The time evolution of both, E_r-shear and the density fluctuations, indicates that the reduction in density fluctuations precedes the increase in the mean E_r-shear. This result seems to be in contradiction with numerous experimental observations supporting the paradigm of mean sheared electric field suppression of turbulence as a unique element to explain transitions to improved confinement regimes. However, a detailed analysis of the signals reveals an increase in the fluctuations of the E_r and E_r-shear within the frequency range 1–10 kHz just at the transition. The increase in the E_r low frequency fluctuations and the reduction in the high frequency density fluctuations are measured a few ms before the mean E_r-shear development, as shown in figure 10. The L–H transition time is indicated in the figure by a vertical line. This example indicates that the turbulence reduction precedes the increase in the mean sheared flow, but it is simultaneous with the increase in the low frequency oscillating sheared flow. This observation may be an indicator, albeit insufficient, of the existence of zonal flows. Additional three-dimensional measurements are required to assess the toroidal and poloidal symmetry of the oscillating sheared flows and their finite radial wavelength. In TJ-II, radial profile of long-range correlation in density and potential fluctuations has been investigated in the scrape-off-layer (SOL) and edge plasma region of the TJ-II stellarator using two Langmuir probe arrays, named probe 1 and probe 2, installed on fast reciprocating drives located at two different toroidal locations. In these experiments probe 1 is moved radially while probe 2 is kept fixed at $r/a \approx 0.9$. The toroidal correlation of density fluctuations is very low. In contrast, the correlation between floating potential signals is significant (up to 0.8); the maximum of the correlation of the floating potential is observed when the probes are approximately at the same radial location in the plasma edge. These results are plotted in figure 11 (left). The radial decay length of long-range correlations towards the SOL region is of the order of 1 cm. It should be noted that long-range correlations due to the emergence of geodesic acoustic modes (GAMs) have been observed both in density and potential fluctuations in different fusion devices, whereas zonal flows do not show significant density fluctuation correlations. Recent experimental findings show that radial transport is reduced in the region dominated by the presence of long-range toroidally correlated structures, which present common characteristics with zonal flows.

The correlation length of the plasma potential becomes of the order of the machine size during the L–H transition,

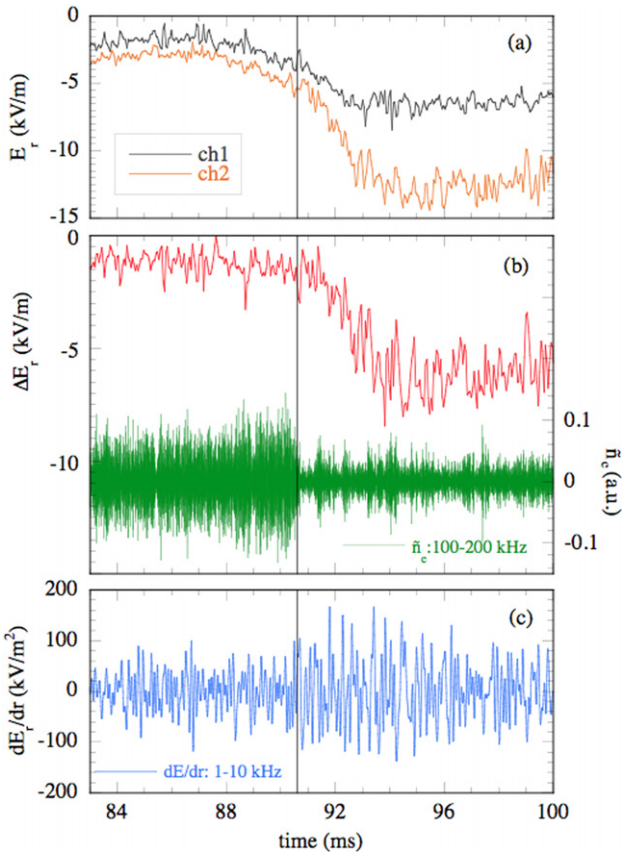

Figure 10. Time evolution of E_r at two adjacent radial positions (a), their difference and the high frequency density fluctuations (b) and the low frequency fluctuations in E_r shear (c); plasma heated by both NBIs in the configuration $\iota(a) = 1.65$. The vertical line indicates the L–H transition time.

quite unlike the density fluctuations [32]. These results show that the increase in the degree of long-range correlation is strongly coupled to the presence of mean radial electric fields. Figure 11 (right) plots the correlation as a function of density in order to see the increase in coherency for the low density and the L–H transitions observed in TJ-II. The observed interplay between mean $E \times B$ shear flows and the development of low frequency (zonal flow like) structures could be explained considering the role of electric fields as a turbulence symmetry-breaking mechanism, i.e. amplifying Reynolds stress driven flows [33].

A fine rotational transform scan performed close to the L–H transition power threshold shows that both the confinement enhancement factor and the shear of the radial electric field increase at the L–H transition by an amount that depends on the magnetic configuration [34]. Both magnitudes show similar ι-dependence (see figure 12): higher values are obtained in certain windows of the edge rotational transform, i.e. in configurations with a low order rational close to the plasma edge. The results indicate a preferential radial position for the rational to ease the transition. Furthermore, the degree of long-range toroidal correlations is modulated during fine dynamical scans in the magnetic configuration in the proximity of low order rational surfaces, consistent with the theory of zonal flows linked to the magnetic topology in low magnetic shear configurations. Changes in transport caused by low order rationals, in the same direction as described here, have also been described in tokamak plasmas [35].

Close to the L–H transition threshold, pronounced oscillations in E_r and density fluctuation level are found to follow a characteristic predator–prey relationship [36]. Differences in the amplitude and duration of these oscillations are found to be associated with different magnetic topologies and/or heating power. The oscillations appear right at the L–H transition and often vanish a few milliseconds later with the subsequent increase in E_r and reduction in the fluctuation level. However, in some configurations the oscillations last for longer time periods giving rise to smoother transitions with lower confinement enhancement factor. The spectrogram of the Doppler reflectometer signal measured during the oscillations is displayed in figure 13. The contour colour map reflects the amplitude of the Doppler peak which is proportional to the density fluctuation level, while the frequency of the Doppler peak gives the radial electric field. These magnitudes, obtained by fitting a Gaussian function to the spectra, are shown in figure 14. The time evolution of both E_r and density fluctuations reveals a characteristic predator–prey behaviour: a periodic evolution with E_r (predator) following the density fluctuation level (prey) with 90° phase difference can be clearly seen. The relation between E_r and the density fluctuation level showing a limit-cycle behaviour is represented in figure 15. For the sake of clarity, only two cycles are displayed. The turbulence induced sheared flow is generated causing a reduction in the turbulent fluctuations (1 in figure 15) the subsequent drop in the sheared flow (2 in figure 15) and the posterior increase in the turbulence level (3 in figure 15). The coupling between fluctuations and flows, described by the above mentioned predator–prey evolution, is consistent with L–H transition models based on turbulence driven flows [37].

5. Conclusions

The recent experimental results are presented in this paper. We have continued with the characterization of plasmas under Li-coating walls, which has allowed the operational density range to be enlarged and H-mode to be reached customarily. The energy confinement time increases substantially for high-density plasmas even in L-mode. The properties of Li on the wall have been studied, including the Li sputtering under H and He plasmas. The sputtering and desorption characteristics of H and He plasmas on a Li surface have been investigated in TJ-II, showing in particular that the thresholds for Li sputtering and for H desorption are very similar in He plasmas, which suggests that both species could obey the same release mechanism. However, a higher mass than that of LiH would still be required to explain the experimental energy values. Laboratory experiments are in progress to check the influence of the underlying B layer on these findings. The properties of fast-ion confinement are also described, showing the appearance of Alfvén modes, as well as the effects of impurities on radiation profiles, showing two types of emissivity profiles the 'bell' and 'dome' shapes, the latter being prone to suffer radiative collapse. The transition from one type of profile to another has been provoked dynamically in a single discharge by impurity puffing.

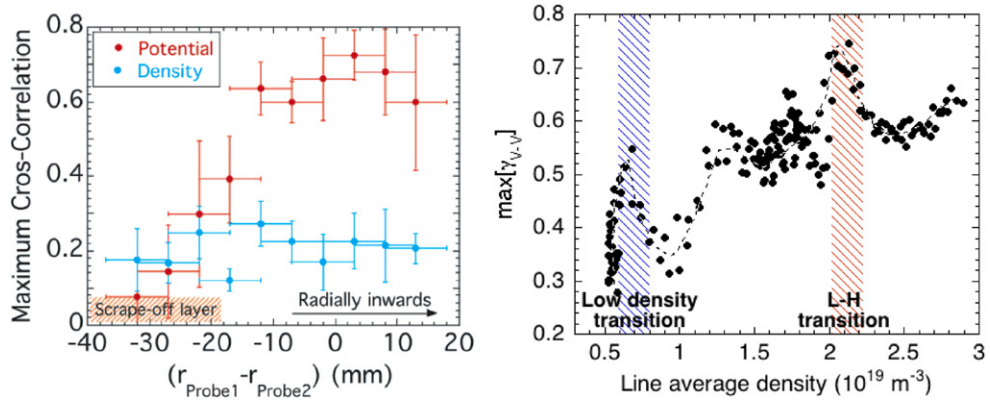

Figure 11. Maximum value of the long-range cross-correlation function for potential fluctuations, as a function of (left) radial position and (right) plasma density.

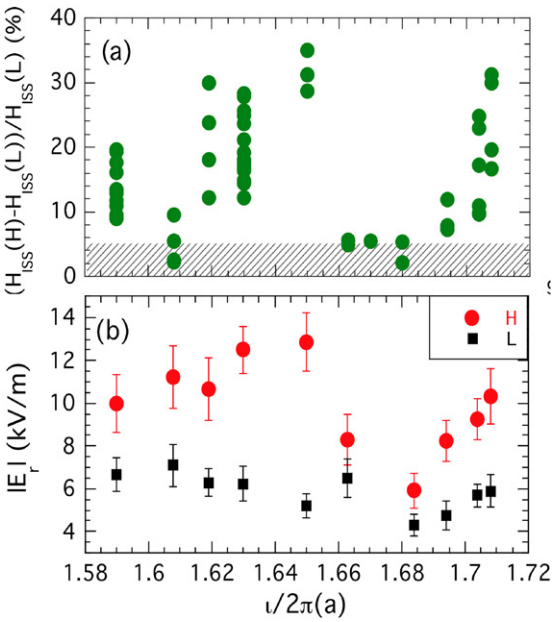

Figure 12. (*a*) Increase in the H factor over the L-mode value and (*b*) absolute value of the radial electric field measured right before the L–H transition (squares) and during the H-mode (circles) at $r = 0.75$–0.8 as a function of edge iota.

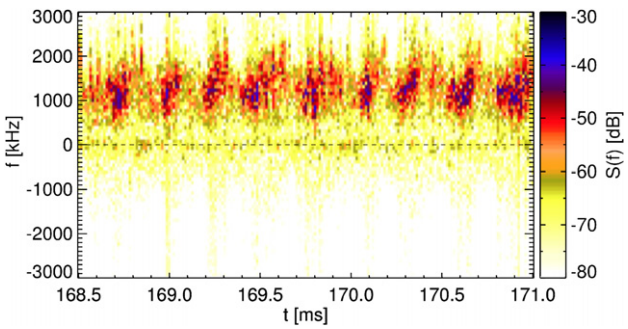

Figure 13. Spectrogram of the Doppler reflectometer signal measured at $\rho \approx 0.8$, in a magnetic configuration with $\iota = 1.53$ at the plasma edge. The colour code reflects the density fluctuation level and the frequency of the Doppler peak gives E_r.

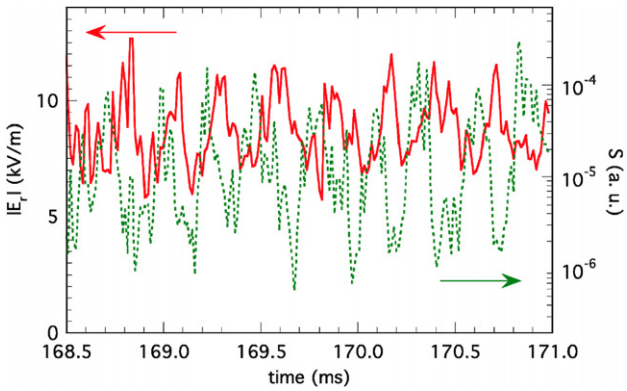

Figure 14. Time evolution of E_r and density fluctuation level obtained from the spectrogram shown in figure 13.

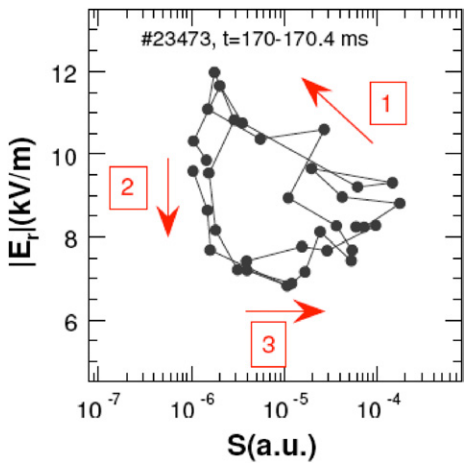

Figure 15. Relation between E_r and density fluctuation level. Only two of the cycles shown in figure 14 are displayed. The time interval between consecutive points is 12.8 μs.

The L–H transitions have shown the development of long-range correlations of the turbulent floating potential in the plasma edge coupled to the presence of mean and fluctuating radial electric fields. These findings provide a new guideline for understanding the trigger mechanisms of the L–H transition, pointing out the importance of low frequency fluctuating sheared $E \times B$ flows. These long-range

toroidal correlations are modulated during fine dynamical scans in the magnetic configuration in the proximity of low order rational surfaces, which is consistent with the theory of zonal flows linked to the magnetic topology. The low order rational surfaces located in the edge also provoke a better quality H-mode. Close to the transition threshold, a coupling between sheared flows and turbulence level is measured which reveals a characteristic predator–prey behaviour consistent with L–H transition models based on turbulence driven flows.

References

[1] Gómez A., Castejón F., Vega-Rodríguez M.A. and Jiménez J.A. 2011 Neoclassical transport optimization in stellarators using a swarm intelligence-based method *Comput. Phys. Commun.* submitted

[2] Happel T. *et al* 2009 Doppler reflectometer system in the stellarator TJ-II *Rev. Sci. Istrum.* **80** 073502

[3] Melnikov A.V. *et al* 2010 Internal measurements of Alfvén eigenmodes with heavy ion beam probing in toroidal plasmas *Nucl. Fusion* **50** 084023

[4] Pedrosa M.A. *et al* 2008 Evidence of long distance correlation of fluctuations during edge transitions to improved confinement regimes in the TJ-II stellarator *Rev. Lett.* **100** 215003

[5] Guzmán F. *et al* 2009 On the determination of edge Ti profiles by a supersonic He beam in TJ-II *J. Nucl. Mater.* **390** 1127

[6] Jiménez-Rey D. *et al* 2008 *Rev. Sci. Instrum.* **79** 93511

[7] Arévalo J., McCarthy K.J., Carmona J.M. and Fontdecaba J.M. 2010 Impurity temperature correction factors for the transmission grating spectrometer in the TJ-II stellarator *Rev. Sci. Instrum.* **81** 10D705

[8] Esteban L., Sánchez M., Sánchez J., Kornejew P., Hirsch M., López J.A., Fernández A. and Nieto-Taladriz O. 2010 Continuous phase measurement in the W7-X IR interferometer by means of an FPGA and high speed ADCs *Fusion Sci. Technol.* **58** 771

[9] Baião D. *et al* 2010 Implementation of multi-filter based twin-prototypes for core electron temperature measurements in the TJ-II stellarator *Rev. Sci. Instrum.***81** 10D711

[10] Vega J., Murari A., Rattá G.A., González S., Dormido-Canto S. and JET-EFDA Contributors 2010 Progress on statistical learning systems as data mining tools for the creation of automatic databases in Fusion environments *Fusion Eng. Des.* **85** 399–402

[11] García-Regaña J.M., Castejón F., Cappa A., Tereshchenko M. and Marushchenko N.B. 2010 Comparison of different models for EBCD calculation in the TJ-II stellarator *Plasma Phys. Control. Fusion* **52** 065007

[12] Velasco J.L. *et al* 2011 Calculation of the bootstrap current profile for the TJ-II stellarator *Plasma Phys. Control. Fusion* submitted

[13] Tabarés F.L. *et al* 2008 *Plasma Phys. Control. Fusion* **50** 124051

[14] Hirooka Y. *et al* 2010 *Nucl. Fusion* **50** 077001

[15] Ascasíbar E. *et al* 2010 Global energy confinement studies in TJ-II NBI plasmas *Contrib. Plasma Phys.* **50** 594

[16] Tafalla D. *et al* 2010 Recycling and sputtering studies in hydrogen and helium plasmas under lithiated walls in TJ-II *J. Nucl. Mater.* at press

[17] Allain J.P., Wgyte D.G. and Brooks J.N. 2004 *Nucl. Fusion* **44** 655

[18] Ochando M.A, Castejón F. and Navarro A.P. 1997 *Nucl. Fusion* **37** 225

[19] Tabarés F.L. *et al* and the TJ-II TEAM 2010 *Contrib. Plasma Phys.* **50** 610

[20] Ochando M.A. *et al* 2010 Nitrogen-injection effects on NBI heated TJ-II plasma profiles under Li wall conditions: impurity screening and role of rational surfaces P1.1075 *37th EPS Conf. on Plasma Physics (Dublin, Ireland, 2010)* http://ocs.ciemat.es/EPS2010PAP/pdf/P1.1075.pdf

[21] Zurro B. *et al* 2011 Perturbation propagation in laser blow-off impurity injection in the TJ-II stellarator and its transport results *Nucl. Fusion* **51** 063015

[22] López-Bruna D. *et al* 2010 Magnetic resonantes in ECR-heated plasmas of the TJ-II Heliac *Contrib. Plasma Phys.* **50** 600

[23] Bondarenko O. *et al* 2010 Influence of low-order rational surfaces on the radial electric field of TJ-II ECH plasmas *Contrib. Plasma Phys.* **50** 605

[24] Narushima Y. *et al* 2011 Experimental study of poloidal flow effect on magnetic island dynamics in LHD and TJ-II *Nucl. Fusion* **51** 083030

[25] Reynolds J.M. and López-Bruna D. 2010 *Phys. Plasmas* **17** 072504

[26] McCarthy K.J., Tribaldos V., Arévalo J. and Liniers M. 2010 The detection of fast oxygen ions in neutral beam heated plasmas of the TJ-II stellarator using spectroscopy methods *J. Phys. B: At. Mol. Opt. Phys.* **43** 144020

[27] Jiménez R. *et al* 2011 Alfvén eigenmodes measured in the TJ-II stellarator *Nucl. Fusion* **51** 033001

[28] Bustos A. *et al* 2011 Fast ion simulations in stellarators *Nucl. Fusion* **51** 083040

[29] Melnikov A. *et al* 2010 HIBP study of Alfvén eigenmodes properties and dynamics in the TJ-II stellarator *Nucl. Fusion* **50** 084023

[30] Estrada T. *et al* 2009 Sheared flows and transition to improved confinement regime in the TJ-II stellarator *Plasma Phys. Control. Fusion* **51** 124015

[31] Happel T. *et al* 2010 On the role of spectral resolution in velocity shear layer measurements by Doppler reflectometer *Rev. Sci. Istrum.* **81** 10D901

[32] Hidalgo C. *et al* 2009 Multi-scale physics mechanisms and spontaneous edge transport bifurcations in fusion plasmas *Europhys. Lett.* **87** 55002

[33] Alonso J.A., Hidalgo C., Pedrosa M.A. and Pablos J.L. 2009 On the link between parallel flows, turbulence and electric fields in the edge of the TJ-II stellarator *Europhys. Lett.* **87** 55002

[34] Estrada T. *et al* 2010 L-H transition experiments in the TJ-II stellarator *Contrib. Plasma Phys.* **50** 501

[35] Austin M.A. *et al* 2006 Core barrier formation near integer q surfaces in DIII-D *Phys. Plasmas* **13** 082502

[36] Estrada T. *et al* 2010 Experimental observation of coupling between turbulence and sheared flows during L-H transitions in a toroidal plasma *Europhys. Lett.* **92** 35001

[37] Diamond P.H. *et al* 1994 Self-regulating shear flow turbulence: A paradigm for the L to H transition *Phys. Rev. Lett.* **72** 2565